https://doi.org/10.5194/egusphere-2026-803
Preprint. Discussion started: 25 February 2026

THEMIS: Spin Axis Magnetic Field Reconstruction

Adrian Pöppelwerth[1], Hans-Ulrich Auster[1], Vassilis Angelopoulos[2], James M. McTiernan[3], James W. Lewis[3], and Ferdinand Plaschke[1]

[1]Institute of Geophysics and Extraterrestrial Physics, TU Braunschweig, Braunschweig, Germany
[2]Department of Earth, Planetary and Space Sciences, University of California Los Angeles, Los Angeles, CA, United States
[3]Space Sciences Laboratory, University of California Berkeley, Berkeley, CA, United States

Correspondence: Adrian Pöppelwerth (a.poeppelwerth@tu-braunschweig.de)

Abstract. The Time History of Events and Macroscale Interactions during Substorms (THEMIS) mission investigates the coupling between the solar wind and Earth's magnetosphere using five identical spinning spacecraft. Each spacecraft rotates at a predefined rate to stabilize it and carries a suite of instruments, including a fluxgate magnetometer (FGM) that measures the three-dimensional magnetic field. Since May 24, 2024, the FGM on board THEMIS E has no longer recorded the magnetic field component along the spin axis, while the two components approximately within the spin plane remain fully available.

We present a method to reconstruct the missing magnetic field component using data from these two remaining components together with the spacecraft spin, yielding full three-component magnetic field vectors at spin-period resolution. The approach was validated using original THEMIS E data from 2017, when all three sensor components were available. The width of the residual distributions between reconstructed and original measurements is approximately 4 nT in the low-field magnetosphere, 12 nT in the high-field magnetosphere, 10 nT near magnetopause crossings, 14 nT in the magnetosheath, 6 nT in the quasi-parallel solar wind, and 3 nT in the quasi-perpendicular solar wind.

These results demonstrate that on a spinning spacecraft, two components that are almost within but slightly out of the spin plane are sufficient to reconstruct three-dimensional magnetic field vectors at spin-period resolution, allowing continued magnetospheric observations despite the loss of one sensor component.

1 Introduction

Continuous and accurately calibrated magnetic field measurements are essential to study the large-scale interaction between the solar wind and Earth's magnetosphere. Magnetometers onboard spacecraft provide these observations and are therefore fundamental for investigating the coupling between interplanetary and terrestrial magnetic fields (e.g., Balogh, 2010).

The Time History of Events and Macroscale Interactions during Substorms (THEMIS) mission (Angelopoulos, 2008) is designed to study these large-scale interactions and consists of five identical spacecraft, each equipped with a fluxgate magnetometer (FGM, Auster et al., 2008). The spacecraft spin at a predefined rate denoted as T_{spin} to stabilize them. The FGM is designed to measure low magnetic fields present in the solar wind as well as the ambient terrestrial magnetic field in close proximity to Earth in three dimensions. One of its sensitive axes is approximately aligned with the spin axis (hereafter referred to as the spin axis sensor), while the other two are nearly aligned with the spin plane (hereafter referred to as spin plane sensors), although they deviate slightly from the exact spin-plane orientation. The three sensors are nearly, but not perfectly, orthogonally aligned.

Careful calibration of the FGM data is required to convert the raw magnetometer output $\boldsymbol{B}_\mathrm{S}$ into physically meaningful magnetic field measurements $\boldsymbol{B}$ (see e.g., Auster et al., 2008; Frühauff et al., 2017; Plaschke et al., 2019). $\boldsymbol{B}_\mathrm{S}$ is recorded in the non-orthogonal sensor coordinate system that co-rotates with the spacecraft. The transformation to $\boldsymbol{B}$ involves several steps: (1) applying gain factors that convert the raw instrument output into physical units, specific to each sensor axis; (2) geometrically transforming the measurements from the non-orthogonal sensor coordinate system into an orthogonal, spin-axis-aligned coordinate system; and (3) subtracting offsets, which represent non-vanishing outputs of the magnetometer in the absence of ambient fields, originating from the instruments themselves and from spacecraft-generated stray fields. This transformation can be expressed as:

$$\boldsymbol{B} = \mathbf{C} \cdot (\boldsymbol{B}_\mathrm{S} - \boldsymbol{O}_\mathrm{S}), \qquad (1)$$

where $\boldsymbol{O}_\mathrm{S}$ denotes the offset vector and $\mathbf{C}$ the coupling matrix, which depends on three gain factors and six orientation angles of the sensor axes.

Recently, the THEMIS E spacecraft (THE) has encountered some challenges, particularly due to radiation damage to the instruments Analog-to-Digital Converter (ADC). Notably, since May 24, 2024, at 22:54:06 UTC, no magnetic field measurements have been obtained from the spin axis sensor. In contrast, the two remaining spin plane sensors continue to operate nominally.

Because the two remaining sensor axes are slightly inclined relative to the spin plane, the missing spin-axis component can be reconstructed from their measurements. In the non-orthogonal sensor coordinate system, which co-rotates with the spacecraft, the magnetic field projected onto each spin plane sensor varies periodically as the spacecraft spins. A magnetic field component within the spin plane therefore appears as a sinusoidal signal, while a constant magnetic field component along the spin axis manifests as a constant offset in the time series. In the despun coordinate time series the constant offset is present as a sinusoidal offset with the spin frequency ω_s and thus referred to as the spin tone (B_ST). Since this spin tone is indistinguishable from the result of a true instrumental offset in the same coordinate system, accurately determining the spin plane offsets is crucial for reconstructing the spin axis signal.

Assuming that the spin plane offsets have been accurately estimated, the amplitude of this spin tone primarily depends on the magnetic field component along the spin axis B_SA and the angle α between a spin plane sensor and the spin axis (Plaschke et al., 2019):

$$B_\mathrm{ST} = B_\mathrm{SA} \cdot \cos\alpha. \qquad (2)$$

In this paper, we present a method to calculate the spin tone and subsequently recover the missing spin axis magnetic field component. We begin by formulating the mathematical basis of the problem, followed by a description of its implementation in the updated calibration process. Finally, we compare the recovered data against measurements from 2017, when all sensor axes were fully operational. The year 2017 was chosen as a trade-off between instrument degradation and temporal proximity

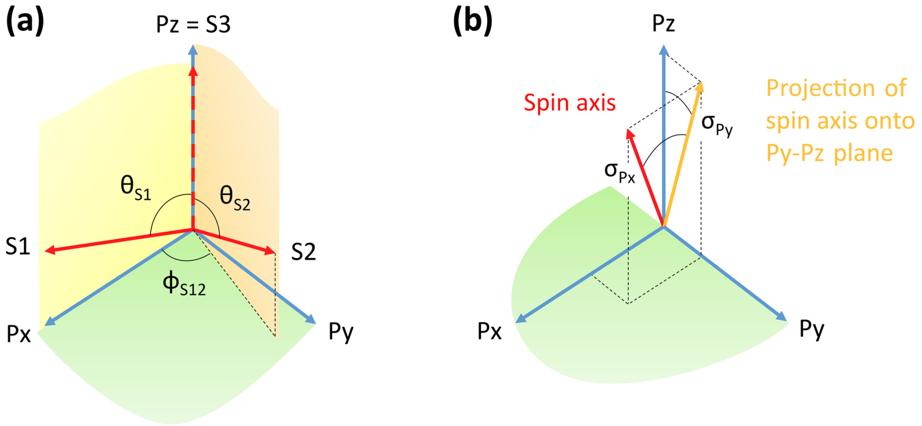

Figure 1. Sketch of coordinate systems: (a) actual sensor axes (in red), orthogonalized sensor axes (in blue), (b) spin axis and rotation angles σ_{px} and σ_{py} in the sensor package system. Fig. 1 from Plaschke et al. (2019).

to the present mission phase. The approach restores the full vector magnetic field at spin-period resolution and thereby extends the THEMIS FGM dataset as a continuous resource for magnetospheric research.

2 Mathematical Background

We first introduce the coordinate systems and derive an expression for α, before describing the determination of B_{ST} from the spin plane measurements.

2.1 Coordinate System and Coupling Matrix

To clarify the geometry of the problem, we follow the formalism introduced by Plaschke et al. (2019), which builds on Kepko et al. (1996). We adopt their notation for consistency, while noting that the final implementation of our coupling matrix **C** differs slightly in form while yielding identical results. The orientation of the three non-orthogonal sensor axes, S1, S2 and S3, is illustrated in red in Fig. 1a. The raw magnetometer output along these axes is transformed into an orthogonal spin-axis-aligned coordinate system (x, y and z) with physical meaningful units using the coupling matrix **C** (see Eq. 1). The coupling matrix can be expressed as

$$\mathbf{C} = \mathbf{\Phi} \cdot \mathbf{\Sigma} \cdot \mathbf{\Gamma} \cdot \mathbf{G}, \tag{3}$$

where each submatrix accounts for a specific step in the coordinate transformation. The conversion matrix $\mathbf{\Gamma}$ transforms the raw, non-orthogonal sensor output into an orthogonal sensor package coordinate system (Px, Py and Pz), represented by the

https://doi.org/10.5194/egusphere-2026-803
Preprint. Discussion started: 25 February 2026

blue axes in Fig. 1:

$$\mathbf{\Gamma} = \begin{pmatrix} \sin\theta_{\mathrm{S1}} & 0 & \cos\theta_{\mathrm{S1}} \\ \cos\phi_{\mathrm{S12}}\sin\theta_{\mathrm{S2}} & \sin\phi_{\mathrm{S12}}\sin\theta_{\mathrm{S2}} & \cos\theta_{\mathrm{S2}} \\ 0 & 0 & 1 \end{pmatrix}^{-1}. \tag{4}$$

The angles θ_{S1}, θ_{S2}, and ϕ_{S12} define the internal geometry of the sensor axes (see Fig. 1a). The subsequent rotation matrix $\mathbf{\Sigma}$ aligns the sensor-package system with the spacecraft spin axis:

$$\mathbf{\Sigma} = \begin{pmatrix} \cos\sigma_{\mathrm{P_x}} & 0 & -\sin\sigma_{\mathrm{P_x}} \\ 0 & 1 & 0 \\ \sin\sigma_{\mathrm{P_x}} & 0 & \cos\sigma_{\mathrm{P_x}} \end{pmatrix} \cdot \begin{pmatrix} 1 & 0 & 0 \\ 0 & \cos\sigma_{\mathrm{P_y}} & -\sin\sigma_{\mathrm{P_y}} \\ 0 & \sin\sigma_{\mathrm{P_y}} & \cos\sigma_{\mathrm{P_y}} \end{pmatrix}, \tag{5}$$

where σ_{Px} and σ_{Py} describe the tilt of the spin axis relative to the sensor package coordinate system (see Fig. 1b). The azimuthal rotation around the spin axis by the angle ϕ_{a} (not shown in Fig. 1) is represented by

$$\mathbf{\Phi} = \begin{pmatrix} \cos\phi_{\mathrm{a}} & -\sin\phi_{\mathrm{a}} & 0 \\ \sin\phi_{\mathrm{a}} & \cos\phi_{\mathrm{a}} & 0 \\ 0 & 0 & 1 \end{pmatrix}. \tag{6}$$

Finally, the gain matrix $\mathbf{G}$ applies the sensor-specific conversion factors into meaningful physical units:

$$\mathbf{G} = \begin{pmatrix} gG_{\mathrm{p}} & 0 & 0 \\ 0 & G_{\mathrm{p}}/g & 0 \\ 0 & 0 & G_{\mathrm{a}} \end{pmatrix}, \tag{7}$$

where g is the ratio of the spin plane gains $G_{\mathrm{S1}}/G_{\mathrm{S2}}$, and $G_{\mathrm{p}}(=\sqrt{G_{\mathrm{S1}}G_{\mathrm{S2}}})$ and G_{a} are the absolute gains for the spin plane and the spin axis sensors, respectively (Plaschke et al., 2019).

Whereas $\mathbf{\Gamma}$ remains nearly constant throughout the mission for a well-constructed magnetometer, the elements of $\mathbf{\Sigma}$ can vary over time due to spacecraft maneuvers that alter the moment of inertia and thereby the spin-axis orientation (for more details on the coupling matrix see Plaschke et al., 2019).

2.2 Determination of the Sensor-to-Spin-Axis Angles

Using the transformation matrices, the angles α_{S1}, α_{S2}, and α_{S3} between each sensor axis and unit vector along the spin axis $\boldsymbol{z}$ $(=[0,0,1]^{\mathrm{T}}$, in the orthogonal spin-axis-aligned coordinate system) can be expressed as

$$\begin{aligned} \begin{pmatrix} \alpha_{\mathrm{S1}} \\ \alpha_{\mathrm{S2}} \\ \alpha_{\mathrm{S3}} \end{pmatrix} &= \cos^{-1}\left(\mathbf{\Gamma}^{-1}\cdot\mathbf{\Sigma}^{-1}\cdot\mathbf{\Phi}^{-1}\cdot\boldsymbol{z}\right) \\ &= \cos^{-1}\begin{pmatrix} \sin\theta_{\mathrm{S1}}\sin\sigma_{\mathrm{P_x}} + \cos\theta_{\mathrm{S1}}\cos\sigma_{\mathrm{P_x}}\cos\sigma_{\mathrm{P_y}} \\ \cos\phi_{\mathrm{S12}}\sin\theta_{\mathrm{S2}}\sin\sigma_{\mathrm{P_x}} + \sin\phi_{\mathrm{S12}}\sin\theta_{\mathrm{S2}}\cos\sigma_{\mathrm{P_x}}\sin\sigma_{\mathrm{P_y}} + \cos\theta_{\mathrm{S2}}\cos\sigma_{\mathrm{P_x}}\cos\sigma_{\mathrm{P_y}} \\ \cos\sigma_{\mathrm{P_x}}\cos\sigma_{\mathrm{P_y}} \end{pmatrix}. \end{aligned} \tag{8}$$

Assuming that θ_{S1}, θ_{S2}, and ϕ_{S12} remain constant, the parameters $\sigma_{\mathrm{P_x}}$ and $\sigma_{\mathrm{P_y}}$ can be derived from Eq. 8 using independently known values of α_{S1}, α_{S2}, and α_{S3} (see Sec. 3 for details).

2.3 Determination of the Spin Tone

To determine the spin tone B_{ST} from the measurements of the spin plane sensor axes data B_{S1} and B_{S2}, we perform a least-squares fit after subtracting the offset vector $\boldsymbol{O}_{\mathrm{S}}$ and converting to physical units by applying the corresponding gain factors:

$$B_{\mathrm{raw},1} = gG\mathrm{p}\left(B_{\mathrm{S1}} - O_{\mathrm{S1}}\right), \tag{9}$$

$$B_{\mathrm{raw},2} = \frac{G_{\mathrm{P}}}{g}\left(B_{\mathrm{S2}} - O_{\mathrm{S2}}\right). \tag{10}$$

This approach allows us to distinguish between the spin-modulated variation within the spin plane and the slowly varying spin tone component. The corresponding fitting function with respect to $B_{\mathrm{raw},1}$ and $B_{\mathrm{raw},2}$ is given by:

$$B_{\mathrm{fit}}(t) = \underbrace{(A + B\cdot t)\cdot\cos\left(\omega_{\mathrm{s}}\cdot(t-\varphi)\right)}_{B_{\mathrm{spinplane}}} + \underbrace{C + D\cdot t}_{B_{\mathrm{ST}}} = B_{\mathrm{spinplane}}(t) + B_{\mathrm{ST}}(t). \tag{11}$$

Here, $\omega_{\mathrm{s}} = 1/T_{\mathrm{spin}}$ denotes the spin frequency, t is the time, $(A + B\cdot t)$ represents the time-varying amplitude of the sinusoidal component of the fit, φ is the phase, and $C + D\cdot t$ is the residual, time-varying offset. The first term $(A + B\cdot t)\cdot\cos\left(\omega\cdot(t-\varphi_{\mathrm{s}})\right)$ corresponds to the measurement of the spin plane magnetic field in the direction of the spin plane sensor axis ($B_{\mathrm{spinplane}}$), while the second term $C + D\cdot t$ represents the amplitude of the spin tone (B_{ST}) in the despun coordinate system.

3 Implementation

In this section, we describe the procedure used to recover the missing sensor measurement along the spin axis. The overall workflow is summarized in the flow chart shown in Fig. 2, with each step and its derived variables explained in the subsequent sections.

We calculate the spin tone B_{ST} from both spin plane sensor components B_{S1} and B_{S2} independently. Between the two, we use the result from the sensor whose axis forms the smaller angle with the spin axis, i.e., the one with the larger value of $|90^\circ - \alpha_{\mathrm{S1,S2}}|$, as the influence of the spin-axis component is more pronounced there.

3.1 Determination of the Spin Tone

First, we use $\boldsymbol{B}_{\mathrm{raw}}$ as obtained from Eq. 9 and 10 as input data. We utilize the low-telemetry channel of the FGM (FGL, for details see Auster et al., 2008), which provides data with sampling rates between 4 and 128 Hz. We do not use the high-telemetry channel (FGH), as it is rarely available, nor the onboard spin-resolution product (FGS) because its resampling removes the spin modulation required for the fit.

We then apply Eq. 11 to the spin plane sensor components of $\boldsymbol{B}_{\mathrm{raw}}$ using a sliding window of 2.5 spin periods, shifted by one spin period between consecutive fits. This procedure yields estimates of the spin tone B_{ST} in spin resolution ($\approx 3-4$ s).

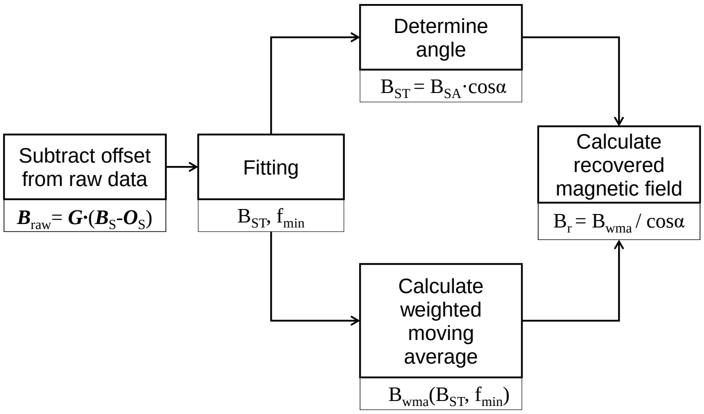

Figure 2. Flow chart illustrating the recovery of the spin axis measurements. The small boxes below each step show which variables are determined. The details of the individual steps are explained in the text.

As a measure of the fit uncertainty, we compute the mean squared difference between B_{fit} and B_{raw} for each window:

$$f_{\text{min}} = \frac{(B_{\text{fit}} - B_{\text{raw}})^2}{n} \tag{12}$$

where n denotes the number of measurement points per window. To suppress the influence of poor fits, we calculate a weighted moving average with a window length L of 1 minute:

$$B_{\text{wma}}(t) = \frac{\sum_{t-L/2}^{t+L/2} B_{\text{ST}}(t)w(t)}{\sum_{t-L/2}^{t+L/2} w(t)}, \tag{13}$$

with the weight $w(t) = A(t)^2/f_{\text{min}}(t)$. The inclusion of the amplitude term A ensures that intervals with large magnetic field magnitudes are not systematically down-weighted, since even small relative deviations can yield large absolute errors in these regions. This relative weighting provides a more consistent quality measure across the entire dynamic range of the observed magnetic field, which ranges from a few nT in the solar wind to more than 10.000 nT near Earth.

3.2 Recovery of the Spin Axis Component

Having obtained the weighted moving average of the spin tone B_{wma}, we reconstruct the missing spin-axis measurement B_{r} by dividing B_{wma} by the factor $\cos\alpha$. This requires accurate knowledge of the angle α between a spin plane sensor and the spin axis. As discussed in Section 2.2, these angles could in principle be derived from the coupling matrix $\mathbf{C}$ (see Eq. 8). However, due to the loss of the spin-axis measurement, a direct in-flight calibration of $\mathbf{C}$ is no longer feasible. This is because the spin tone minimization used in the regular calibration process can no longer uniquely distinguish whether a residual spin tone originates from the true spin-axis signal, from remaining spin-plane offsets, or from inaccuracies in the angular terms of $\mathbf{C}$.

The orientation of the spin axis changes due to gravity gradient effects and performing orbital maneuvers, and thus the effective coupling matrix, changes over time, making it necessary to update these parameters continuously. To estimate the angles α_{S1} and α_{S2}, we therefore use Eq. 2 in combination with the fitted spin tone B_{ST} and a modeled magnetic field approximation for the spin-axis component B_{SA}. The angle determination is restricted to perigee intervals, where the high magnetic field strength ensures that small perturbations have only a minor relative impact on the derived angles, as any residual sensor offsets and their uncertainties become negligible in comparison. We define the perigee region by a minimum field strength of $10,000$ nT.

As model field we use the International Geomagnetic Reference Field (IGRF) superposed with the model field of Tsyganenko (1989), hereafter referred to as T89. The IGRF, which represents the internal part of the Earth's magnetic field, is a good approximation of the actual terrestrial magnetic field near perigee (e.g. Alken et al., 2021), while the T89 model provides a simple and widely used empirical description of the external magnetospheric field, parameterized by the geomagnetic k_{p} index (Matzka et al., 2021).

The comparison between B_{ST} and B_{SA} yields updated estimates of α_{S1} and α_{S2} (cf. Eq. 2). These are then used in a least-squares optimization of the parameters σ_{Px} and σ_{Py} (cf. Eq. 8), ensuring continued calibration of the coupling matrix $\mathbf{C}$ throughout the mission. Since May 2024, the angles between the spin axis and the two sensor axes have been $90.9°$ and $89.8°$ for α_{S1} and α_{S2}, respectively.

As discussed in Appendix A, additional efforts were made to further refine and improve the recovered spin axis signal. However, the analysis reveals that such attempts not only proved challenging but also led to inconsistent results. Therefore, we consider B_{r} as the final data product used to replace the missing spin axis measurement. It should be noted that deviations between the original measurements and the recovered signal remain, which are analyzed and discussed in the following sections.

4 Comparison of Results

To validate the accuracy of the recovery method, we compare the recovered magnetic field component with original measurements from THE for year 2017 (when the angles α_{S1} and α_{S2} were $91.8°$ and $89.5°$, respectively), and with data from THA as reference spacecraft for periods after the loss of the spin axis sensor component measurements (since May 2024).

4.1 Qualitative Comparison

In Fig. 3 we present two representative qualitative comparisons from 2017: one interval from the magnetosphere from 24 April (Fig. 3a) and one from the magnetosheath including multiple magnetopause crossings from 29 July (Fig. 3b). In both panels, the original measurement B_{FGS}, recovered data B_{r}, and model field B_{T89} are shown in black, red, and blue, respectively. In Fig. 3a the recovered data closely follow the original measurements, with differences primarily arising from the smoothing of

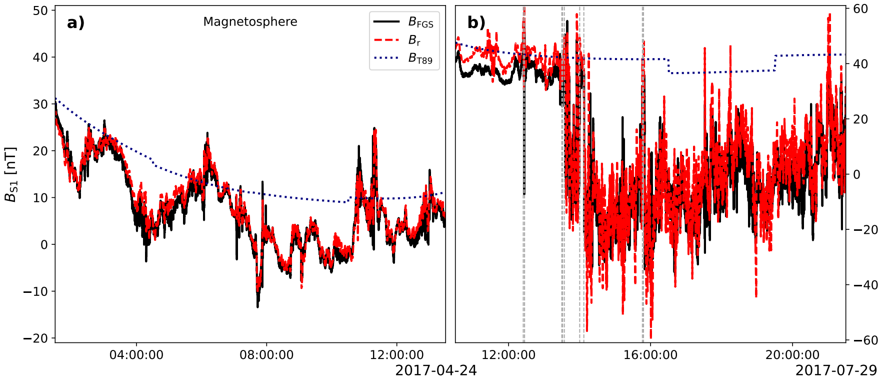

Figure 3. Comparison between recovered (B_r, red), original (B_FGS, black), and model (B_T89, blue) magnetic field data for (a) a magnetospheric interval and (b) a magnetosheath interval following multiple magnetopause crossings (vertical gray lines) in 2017. The original data correspond to calibrated FGS measurements from THE.

B_r introduced by the recovery process. Figure 3b presents data where THE traversed the magnetopause multiple times between 12:24 UTC and 15:48 UTC. Magnetopause crossings, identified using the list from Grimmich et al. (2023), are indicated by vertical gray lines. The recovered data also generally follow the original measurements, though larger deviations are observed during boundary crossings and within the magnetosheath, where the magnetic field changes rapidly. Notably, in both examples B_r provides a far better representation of the observed field than the model field B_T89, which remains valid only within the magnetosphere.

Following the validation with original 2017 measurements, we next evaluate the recovery after the spin axis component became unavailable in May 2024 by comparing the recovered data B_r with simultaneous observations from the nearby reference spacecraft THA. Two representative intervals are shown in Fig. 4: magnetosheath observations prior to a magnetopause crossing from 8–9 June 2024 (Fig. 4a) and magnetosphere observations from 28–29 November 2024 (Fig. 4b). In both panels, the reference measurements from THA B_FGS, B_r, and B_T89 are displayed in black, red, and blue, respectively. The recovered data generally reproduce the reference measurements in both intervals, although enhanced deviations occur near the magnetopause and within the turbulent magnetosheath (Fig. 4a). In the magnetosphere interval (Fig. 4b), discrepancies are visible between 02:45-03:30 and 06:00-08:30 UTC, which may reflect spatial separation between THE and THA ($\approx 1\ R_\mathrm{E}$). Without the original spin axis measurements from THE, this cannot be verified. In both examples, within the magnetosphere the recovered data provide a substantially better representation of the observed reference field than the model B_T89.

4.2 Quantitative Comparison

The examples suggest that the accuracy of the recovery depends on the spacecraft's plasma environment. To quantify this dependence, we assess the performance of the recovery method in different regions of near-Earth space. Specifically, we divide the 2017 data set into the following regions: the magnetosphere, the magnetopause, the magnetosheath, and the solar wind.

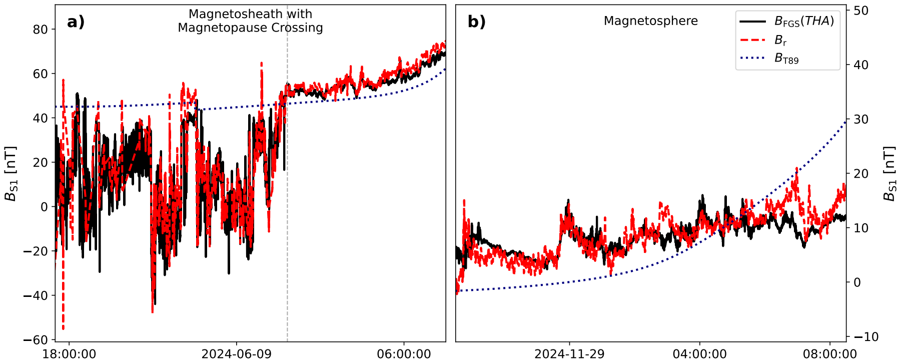

Figure 4. Comparison between recovered (B_r, red), reference spacecraft (B_FGS, black), and model (B_T89, blue) magnetic field data in (a) the magnetosheath before a magnetopause crossing at 01:49 UTC (vertical gray line) and (b) the magnetosphere in 2024. The reference data correspond to calibrated FGS measurements from THA, since spin axis measurements from THE are no longer available.

The solar wind is further subdivided into quasi-parallel and quasi-perpendicular regions upstream of the bow shock. Within the magnetosphere, we distinguish between low ($|B_\mathrm{FGS}| < 50$ nT) and high field ($B_\mathrm{FGS} > 50$ nT) intervals. To identify the different regions, we use the results from Edmond et al. (2024) who applied a combination of unsupervised machine learning methods to classify THEMIS observations into magnetosphere, magnetosheath, and solar wind observations. We make use of their publicly available 2017 dataset for THE, in which each data point is assigned to one of these regions. Magnetopause and bow shock crossings are identified by changes in the region label. In addition, to further divide the data set, we also use magnetic field data from the FGM (fully operational in 2017) and the omni directional ion energy flux E_flux (ESA, McFadden et al., 2008).

Magnetospheric data are separated into low- and high-field intervals to avoid biasing the statistics, as larger absolute deviations are expected close to perigee where the magnetic field is strongest. We define the low field magnetosphere by data points that fulfill $|B_\mathrm{FGS}| < 50$ nT and are labeled as magnetosphere. Data points in the magnetosphere for which 50 nT $< B_\mathrm{FGS}$ are applicable belong to the high field magnetosphere. Data within ±15 min of each magnetopause crossing are attributed to the magnetopause region. The magnetosheath is defined by the machine learning labels, except for the points near the magnetopause crossings. The solar wind data set is used as specified by the model and then divided into quasi-parallel and quasi-perpendicular by having E_flux at 10 keV higher and lower than $20{,}000\ \mathrm{cm}^{-2}\mathrm{s}^{-1}\mathrm{sr}^{-1}$, respectively. Manual inspection confirmed the robustness of these assignments, with few outliers that were removed from the subsets.

We observe 2,397,045 and 951,265 data points in the low and high field magnetosphere, 246,609 data points around the magnetopause, and 674,122 in the magnetosheath, respectively. In the solar wind, however, we observe only 80,358 and 30,008 data points in the quasi-parallel and quasi-perpendicular regions, respectively. The large differences in the data quantities can be attributed to the orbital configuration of the THEMIS mission.

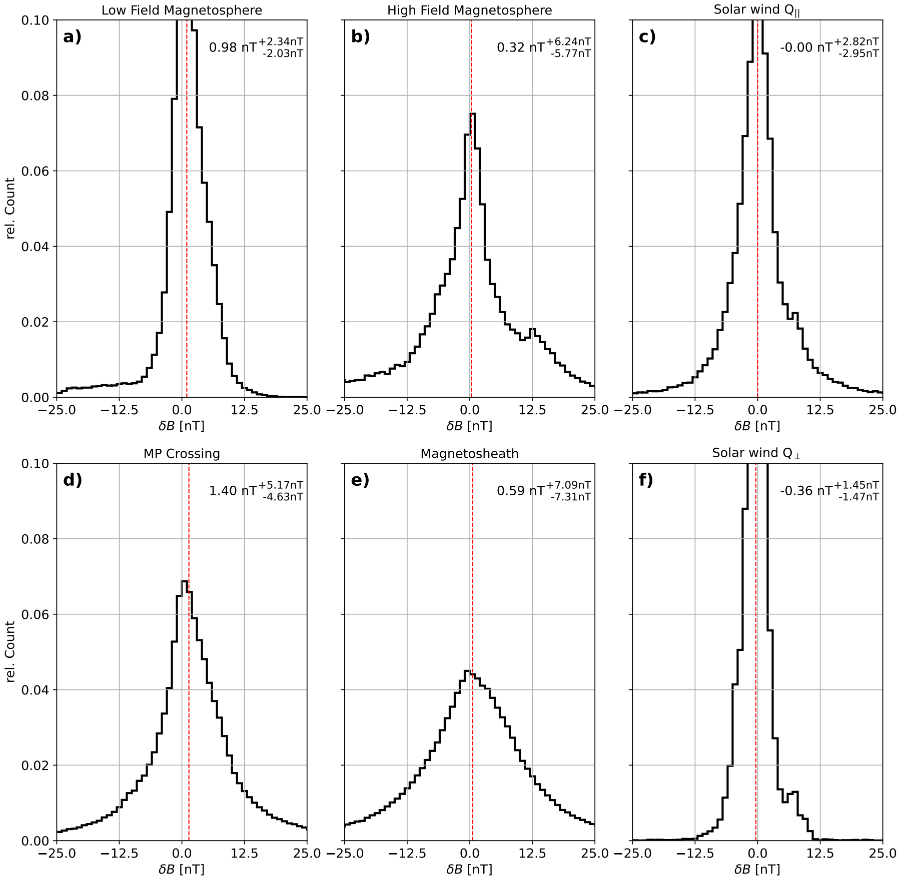

Figure 5. Histograms of the deviation δB between recovered (B_r) and original (B_FGS) spin-axis measurements in six different regions: (a) low-field magnetosphere near perigee, (b) high-field magnetosphere, (c) quasi-parallel solar wind, (d) magnetopause crossings, (e) magnetosheath, and (f) quasi-perpendicular solar wind. The vertical red dashed lines indicate the median values, and the ± values correspond with the 25th and 75th percentiles.

For each region, we calculate the difference between the recovered B_r and the original spin axis measurements B_FGS:

$$\delta B = B_\mathrm{r} - B_\mathrm{FGS}. \tag{14}$$

The distributions of δB for the different regions are shown in Fig. 5.

Figure 5a shows δB for the low-field magnetosphere. The distribution is nearly centered around zero, with a slight positive shift and a median value below 1 nT. In the high-field magnetosphere (Fig. 5b), the distribution is broader but still centered near zero, with a median value below 0.5 nT. Near the magnetopause (Fig. 5d) and in the magnetosheath (Fig. 5e), the distributions are comparable in shape to the high-field magnetosphere but exhibit higher median values, above 1 nT and above 0.5 nT, respectively. In the solar wind, both the quasi-parallel and quasi-perpendicular cases (Fig. 5c and Fig. 5f) show narrow distributions centered near zero, with median values below 0.5 nT.

https://doi.org/10.5194/egusphere-2026-803
Preprint. Discussion started: 25 February 2026

The position of the median reflects the quality of the spin plane offset determination, with correctly chosen offsets resulting in median values close to zero. The width of the distributions, in contrast, reflects the quality of the fit and of the recovery method, with broader distributions indicating poorer performance. Larger deviations between the recovered and original measurements occur in the high-field magnetosphere, as reflected by the larger interquartile range (> 10 nT). This is expected since absolute differences become more pronounced at higher field strengths, where small relative calibration errors or filter effects can lead to larger absolute deviations.

The smallest absolute deviations are observed in the solar wind with interquartile ranges < 6 nT. The slightly larger deviations in the quasi-parallel case can be attributed to the enhanced turbulence and wave activity in the foreshock region, which complicate the fitting process (see Section 5). The distributions in the magnetosheath and around magnetopause crossing, however, are markedly broader. Their interquartile ranges are comparable to those of the high-field magnetosphere (> 9 nT), even though the magnetic fields themselves are much weaker. These two broader distributions can be explained due to faster changes and higher fluctuation levels in the magnetic field, which likewise complicate the fitting process there.

5 Discussion of Limitations

The accurate determination of the spin plane sensor offsets is essential for deriving reliable spin tone values (B_{ST}) and, consequently, for reconstructing the spin axis signal. Errors in the spin plane offsets directly translate into errors in B_{ST} and thus into errors in the recovered spin axis component. This effect is amplified because the angles between the spin plane sensors and the spin axis are close to 90°, such that even small offset errors can lead to large errors in the recovered spin axis magnetic field.

In the past, spin plane offsets were calibrated by minimizing B_{ST} using the information from the spin axis sensor itself (Plaschke et al., 2019). With the loss of the spin axis measurements, this approach is no longer possible. Likewise, alternative calibration techniques such as the Hedgecock method (Hedgecock, 1975) cannot be applied in the absence of three fully operational sensor components. As a result, the spin plane offset calibration must now rely on model magnetic field values as a proxy for the missing spin axis measurements. This introduces an additional source of uncertainty and makes the recovery process fundamentally dependent on both the accuracy of the magnetic field model and the long-term stability of the FGM instrument. To mitigate these effects, spin plane offsets are adjusted only during intervals within the magnetosphere when the magnetic field shows no sign of significant wave activity, where the magnetic field is relatively stable and model uncertainties are minimized. Nevertheless, this limitation should be considered when interpreting the recovered data.

In addition to these model related uncertainties, we observe systematic deviations of the recovered signal compared to the original measurements after several perigee passages. These deviations frequently coincide with spacecraft eclipse periods when the spacecraft passes through Earth's shadow. During these intervals, the spacecraft experiences strong temperature gradients that affect the offset vector. This effect has been observed throughout the mission and does not originate from the recovery method itself. As a result, the spin plane offsets can fluctuate, leading to inaccurate spin tone determinations. A

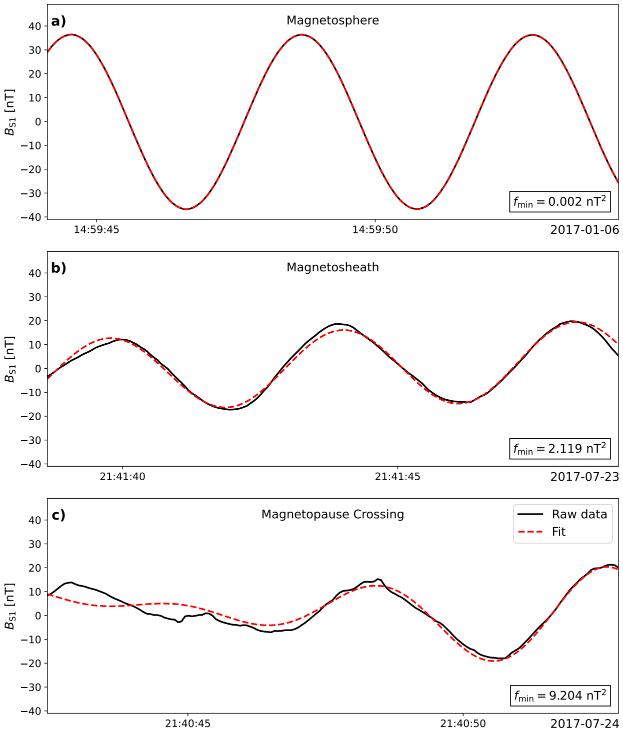

Figure 6. Comparison of fitted and raw spin plane data. In all panels, the raw data are shown in black and the fit as red dashed line. From top to bottom, we present examples for the magnetosphere (a), magnetosheath (b), and a magnetopause crossing (c). The $f_{\rm min}$ value in the lower right corner of each panel quantifies the fit uncertainty (see Eq. 12).

detailed analysis of this effect and attempts to mitigate it are presented in Appendix A. This limitation should be considered when interpreting the recovered data.

Another limitation, although less critical than the previously discussed effects, concerns the quality of the fit and, consequently, the accuracy of the estimated spin tone. In regions with low turbulence, such as the inner magnetosphere or the quiet solar wind, the fits reproduce the periodic spin modulation accurately. However, in highly turbulent environments, such as near boundary crossings or within the magnetosheath (e.g. Lucek et al., 2005), the fit quality degrades. This is reflected in the broader distributions of δB observed at the magnetopause (Fig. 5d) and in the magnetosheath regions (Fig. 5e). To illustrate this behavior, Fig. 6 shows three representative examples of the fitting performance in different plasma regions: in the magnetosphere Fig. 6a, in the dayside magnetosheath Fig. 6b and at a magnetopause crossing Fig. 6c.

The visual comparison confirms that the fitting procedure performs best in the magnetosphere and less reliably near boundary crossings. This is also reflected in the increasing values of $f_{\rm min}$ (see Eq. 12), which quantify the fit uncertainty: from < 0.1 nT^2 in the magnetosphere to ≈ 2 nT^2 in the magnetosheath and ≈ 10 nT^2 at the magnetopause crossing.

In addition to the reduced accuracy of the recovered spin axis signal, the recovery process also decreases the temporal resolution of the data. Even without smoothing, the sampling rate is reduced from 4–128 Hz to maximally one data point per spin period (approximately 3–4 s). The subsequent application of a moving average, which effectively acts as a low-pass filter, further decreases the temporal resolution to half the window length ($L = 60$ s).

6 Conclusions

After more than 17 years in space, the THEMIS E spacecraft stopped recording magnetic field measurements along its spin axis since May 24, 2024, at 22:54:06 UTC. We present a method to reconstruct the missing magnetic field component along this axis. By exploiting the spacecraft's spin motion, we extract information about the missing spin axis component from the spin plane sensor measurements. Specifically, we derive the spin tone B_{ST} by fitting the magnetic field data from the spin plane sensors. Combined with the angle α between the spin axis and the spin plane sensor orientations, obtained from comparisons with the T89 magnetic field model around perigee, we are able to recover the spin axis signal B_{r}.

We use original measurements and recovered data from 2017 to evaluate the reconstruction. The comparison demonstrates that the recovery performs well across different plasma regions. The width of the δB distributions, which reflects the overall quality of the fit and recovery process, is on the order of a few nT in most regions: approximately 4 nT in the low-field magnetosphere, 12 nT in the high-field magnetosphere, about 10 nT near magnetopause crossings, and around 14 nT in the magnetosheath. In the solar wind, the distributions are narrower, with widths of roughly 6 nT in the quasi-parallel and 3 nT in the quasi-perpendicular case.

Since the loss of the spin axis sensor component in May 2024, reconstructed magnetic field data have been made publicly available, with a delay to allow for careful processing and calibration. After reconstructing the spin axis component, the data is converted into raw magnetometer output at spin resolution. The artificially reconstructed raw data is uploaded as a separate Level 1B product for public access (https://themis.ssl.berkeley.edu/data/themis/the/l1b/). This data should be interpreted with caution, ideally taking into account the measurements from the neighboring THA and THD spacecraft.

For future missions, a larger intentional deviation of sensor axes from the spin plane would further improve the ability to recover data in the event of sensor loss. For example, repeating the analysis for the year 2017 after rotating the sensor geometry to a deviation of about $45°$ reduces the distribution widths to $\lesssim 1$ nT in the magnetosphere and solar wind and to $\lesssim$3 nT even near magnetopause crossings and in the magnetosheath. Despite the discussed limitations, we demonstrate that the recovery of magnetic field measurements is possible. Hence, our approach provides a viable solution for the recovery of spin axis measurements, supporting the scientific goals of the magnetometer. This is enabled by a slight misalignment of the spin plane sensor axes from the actual spin plane. Consequently, the inherent spinning motion of the spacecraft proves beneficial not only for routine calibration, but also for measurement recovery.

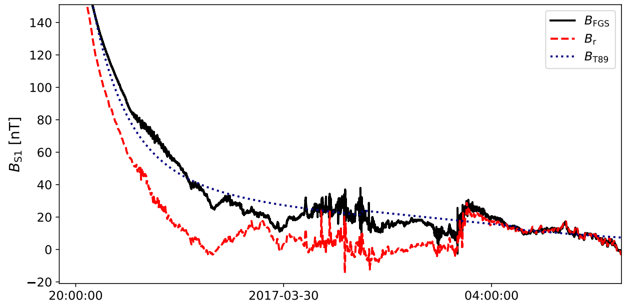

Figure A1. Comparison of recovered and original spin-axis data shortly after a perigee pass. Larger deviations between the two are visible between 20:20 UTC on April 29 and 03:20 UTC on April 30, 2017, decreasing with increasing distance from perigee as the spacecraft approaches apogee.

Code and data availability. Data from the THEMIS mission including FGM and ESA data are publicly available from the University of California, Berkeley, and can be obtained from https://themis.ssl.berkeley.edu/data/themis (THEMIS, 2026). THEMIS data were accessed using the SPEDAS (Angelopoulos et al., 2019, 2024) and PySPEDAS software (Grimes et al., 2018). The software for the revocery process can be found at https://doi.org/10.5281/zenodo.18594248] (Pöppelwerth, 2026).

Appendix A: Additional Cross Correlation Offset

We frequently observe systematic deviations between recovered and original magnetic field data following perigee passes. As discussed in Sect. 5, these deviations appear correlated with temperature gradients that affect the offset behavior. A representative example of the deviations is shown in Fig. A1.

We tested a cross-calibration approach with the other two inner THEMIS probes, THA and THD, to correct for these deviations. Both spacecraft follow orbits that are very similar to that of THE, although they may be shifted along the orbit by a time lag τ. Because of this orbital similarity, all three spacecraft should observe comparable magnetic fields, and consequently also similar deviations between the measurements and the model field.

Based on this idea, we compare the differences between the model field and the recovered magnetic field for THE with the corresponding differences between the model and the measured fields on THA and THD. These differences can be compared either instantaneously (i.e., at the same time) or after shifting the THA/THD data by the lag τ so that the spacecraft are compared at approximately the same orbital position.

Which of the two comparisons is more meaningful depends on the separation between the spacecraft. When they are close together (e.g., near apogee), temporal variations dominate, making the instantaneous comparison more appropriate. At larger separations, spatial variations become more important, and comparing the shifted differences is preferable.

Therefore, we construct a distance-dependent linear combination of the instantaneous and the shifted differences. The method is applied only within the magnetosphere, where the model field remains valid.

https://doi.org/10.5194/egusphere-2026-803
Preprint. Discussion started: 25 February 2026

To implement this approach, we first compute, for each spacecraft, the component of the model magnetic field (IGRF + T89) in the direction of the spin axis of THE. These quantities are denoted as $B_{\mathrm{T89,A}}$, $B_{\mathrm{T89,D}}$, and $B_{\mathrm{T89,E}}$ for THA, THD, and THE, respectively. Likewise, the measured magnetic field vectors from THA and THD ($B_{\mathrm{FGS,A}}$, $B_{\mathrm{FGS,D}}$) are projected onto the same direction. To determine the relative orbital shift between the spacecraft, we compute the cross-correlation between the radial distances $|\boldsymbol{r}_{\mathrm{A/D}}|$ and $|\boldsymbol{r}_{\mathrm{E}}|$ for time lags between -3 h and +3 h. The time lag corresponding to the maximum cross-correlation defines the orbital shift τ. Their orbits are considered sufficiently similar if the maximum cross-correlation coefficient r exceeds 0.8.

Using this lag τ, we compute the two types of deviations between the measurements and the model field: the instantaneous difference ΔB_{t} and shifted difference ΔB_{s}:

$$\Delta B_{\mathrm{s}}(t) = B_{\mathrm{FGS}}(t-\tau) - B_{\mathrm{T89}}(t-\tau), \tag{A1}$$

$$\Delta B_{\mathrm{t}}(t) = B_{\mathrm{FGS}}(t) - B_{\mathrm{T89}}(t). \tag{A2}$$

To combine these contributions depending on spacecraft separation, we introduce a weighting factor

$$\varepsilon = \frac{1}{2}\tanh\left(\frac{d-d_0}{W}\right) + \frac{1}{2}, \tag{A3}$$

where d is the instantaneous separation between THE and the reference spacecraft, d_0 denotes the transition between close proximity and larger separation between the spacecraft, and W controls the width of this transition. The distance-dependent deviation between measurement and model for each reference spacecraft is then given by

$$\Delta B_{\mathrm{A}}(t) = (1-\varepsilon_{\mathrm{A}}) \cdot \Delta B_{\mathrm{t,A}}(t) + \varepsilon_{\mathrm{A}} \cdot \Delta B_{\mathrm{s,A}}(t), \tag{A4}$$

$$\Delta B_{\mathrm{D}}(t) = (1-\varepsilon_{\mathrm{D}}) \cdot \Delta B_{\mathrm{t,D}}(t) + \varepsilon_{\mathrm{D}} \cdot \Delta B_{\mathrm{s,D}}(t), \tag{A5}$$

and the deviation between recovered and model magnetic field for THE is given by

$$\Delta B_{\mathrm{E}}(t) = B_{\mathrm{r}}(t) - B_{\mathrm{T89,E}}(t). \tag{A6}$$

All deviations $\Delta B_{\mathrm{A/D/E}}$ are subsequently smoothed using a one-hour running average to suppress short-term fluctuations. The cross-calibration offset in spin-axis direction is then defined as

$$\delta_{\mathrm{off}}(t) = \Delta B_{\mathrm{E}}(t) - \frac{\Delta B_{\mathrm{A}}(t) + \Delta B_{\mathrm{D}}(t)}{2}. \tag{A7}$$

If only one reference spacecraft (THA or THD) satisfies the correlation threshold ($r > 0.8$), then only that spacecraft is used in Eq. A7. Subtracting δ_{off} from the recovered spin-axis signal B_{r} should, in principle, mitigate the systematic deviations.

The parameters d_0 and W of the weighting factor ε are not predefined and must be determined empirically. To identify suitable values, we performed a parameter study across a two-dimensional grid of parameter pairs: d_0 varied from 1,000 to 50,000 km in steps of 500 km, and W from 250 to 25,000 km in steps of 250 km. For each parameter combination, we computed the cross-calibration offset δ_{off} and evaluated the resulting residual magnetic field difference for THE

$$R_{\mathrm{B}}(t) = B_{\mathrm{r}}(t) - \delta_{\mathrm{off}}(t) - B_{\mathrm{FGS,E}}(t). \tag{A8}$$

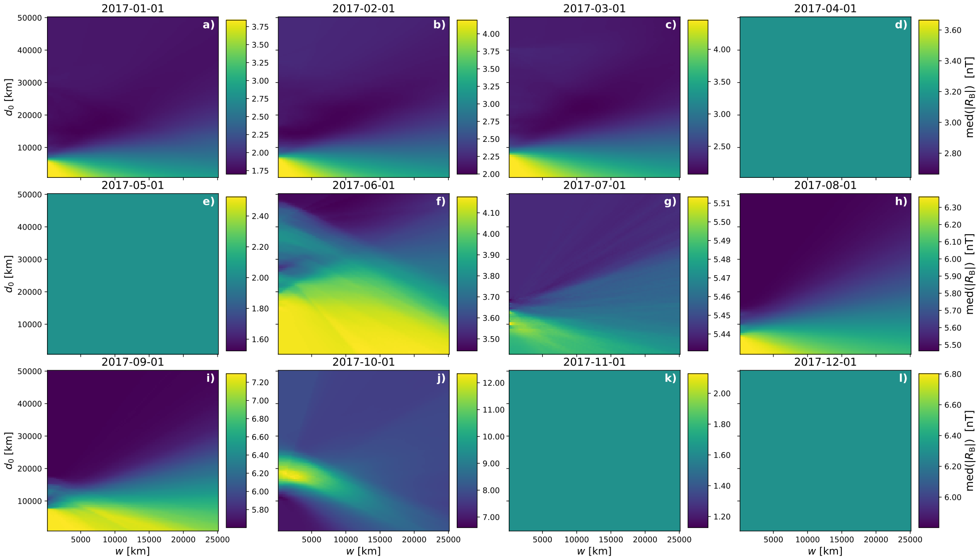

Figure A2. Color-coded representation of the absolute median residual R_B for January (a) to December (l) 2017 as a function of the parameters d_0 and W.

We then calculated the median of the absolute residual $|R_\mathrm{B}(t)|$ over an entire month, denoted by $\mathrm{med}(|R_\mathrm{B}|)$, yielding one representative value per parameter combination and month. Only data points classified as magnetosphere by the list of Edmond et al. (2024) were used, since the T89 model field is valid only in that region. Figure A2 summarizes the results for all months of 2017.

During April, May, November, and December 2017, the cross-correlation between THE and the reference spacecraft did not exceed the required threshold, and no cross-calibration offset was computed for these months. The remaining months exhibit different dependencies of the median residuals on the parameters d_0 and W. January, February, March, August, and September display broadly similar patterns, whereas June, July, and October show strong deviations. However, applying this approach after the spin axis measurements became unavailable would require a stable parameter choice.

To assess whether the additional cross-calibration offset improved the reconstruction, we need to compare the results without the cross calibration applied. Therefore, we calculate difference between B_r and B_FGS (i.e., the baseline residual without cross-calibration)

$$R_\mathrm{B,base}(t) = B_\mathrm{r}(t) - B_\mathrm{FGS,E}(t), \tag{A9}$$

and calculate the median of the absolute residuals $|R_\mathrm{B,base}(t)|$ over an entire month, denoted by $\mathrm{med}(|R_\mathrm{B,base}|)$. For the comparison we subtract $\mathrm{med}(|R_\mathrm{B,base}|)$ from $\mathrm{med}(|R_\mathrm{B}|)$ for each month and value pair:

$$\Delta R = \mathrm{med}(|R_\mathrm{B}|) - \mathrm{med}(|R_\mathrm{B,base}|). \tag{A10}$$

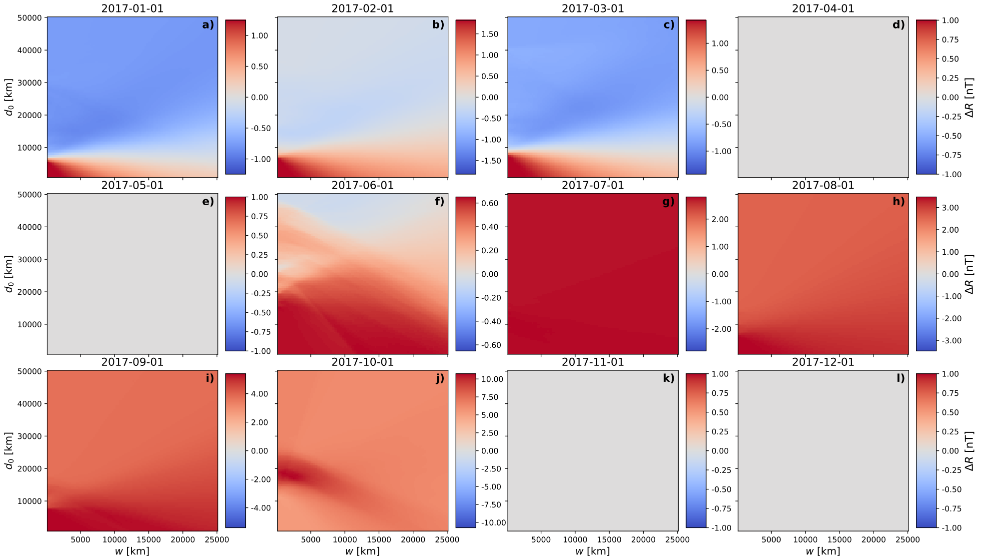

Figure A3. Color-coded representation of the absolute median residual R_{B} subtracted by the absolute median difference between B_{r} and B_{FGS} for for January (a) to December (l) 2017 as a function of the parameters d_0 and W.

The results are displayed in Fig. A3. The color scale indicates the difference between the residuals obtained with and without applying δ_{off}. Negative values (blue) correspond to an improvement due to cross-calibration, whereas positive values (red) indicate a degradation. As seen in Fig. A3, improvements occur mainly in January, February, March, and June 2017, while no improvement is found in the remaining months.

The underlying reason is illustrated in Fig. A4. The deviations between the measured and modeled magnetic fields are not consistent between THE and the other spacecraft (shown here for THA). This violates the core assumption of the cross calibration approach, that the deviations should be comparable at similar orbital locations.

Figure A2 further shows that the optimal parameter combination is not stable over time. Given this inconsistency and the fact that such a parameter study cannot be performed once the spin axis measurements became unavailable, we chose the simpler and more robust approach: omitting the cross-calibration offset entirely and instead advising users to treat the post-perigee deviations with appropriate caution.

Author contributions. AP conceived the analysis and drafted the manuscript. FP contributed significantly to improving the conceptual framework. HUA, VA, JM, JL and FP contributed through discussions and interpretation of the results.

Competing interests. The authors declare that they have no conflict of interest.

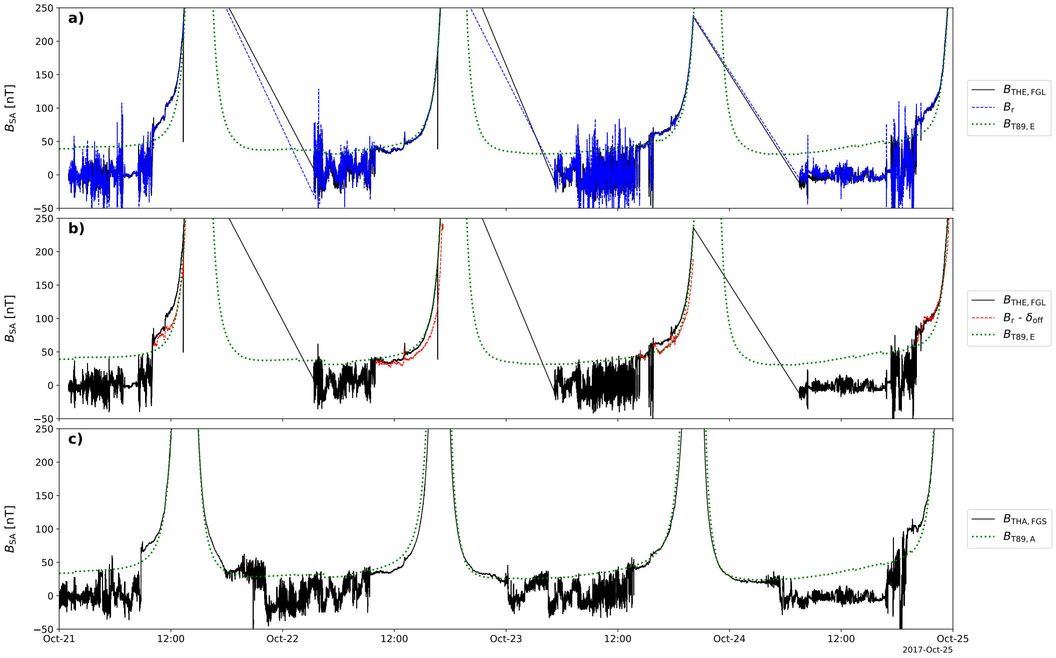

Figure A4. (a): Comparison of original ($B_{\mathrm{THE,FGL}}$, black), model (B_{T89}, green) and recovered (B_{r}, blue) magnetic field data for THE. (b): Comparison of original ($B_{\mathrm{THE,FGL}}$, black), model (B_{T89}, green) and recovered magnetic field data with the cross calibration offset ($B_{\mathrm{r}} - \delta_{\mathrm{off}}$, blue) for THE. (c): Comparison of ($B_{\mathrm{THA,FGS}}$, black) and model (B_{T89}, green) magnetic field data for THA.

Acknowledgements. We acknowledge NASA contract NAS5-02099 for use of data from the THEMIS Mission, specifically C.W. Carlson and J. P. McFadden for the use of ESA data; K. H. Glassmeier, U. Auster, and W. Baumjohann for the use of FGM data provided under the lead of the Technical University of Braunschweig and with financial support through the German Ministry for Economy and Technology and the German Center for Aviation and Space (DLR) under contract 50 OC 0302. This work was financially supported by the German Center for Aviation and Space (DLR) under contract 50 OC 2201. AI tools were used in the process of this work: GitHub Copilot (https://github.com/features/copilot) with Claude Sonnet and newer (https://www.anthropic.com/claude/sonnet) for code suggestions and ChatGPT-4o and newer (https://chatgpt.com/en-EN/overview/) for limited help with wording and grammar during the preparation of this manuscript.

https://doi.org/10.5194/egusphere-2026-803
Preprint. Discussion started: 25 February 2026

References

Alken, P., Thébault, E., Beggan, C. D., et al.: International Geomagnetic Reference Field: the thirteenth generation, Earth, Planets Space, 73, https://doi.org/10.1186/s40623-020-01288-x, 2021.

Angelopoulos, V.: The THEMIS Mission, Space Sci. Rev., 141, 5–34, https://doi.org/10.1007/s11214-008-9336-1, 2008.

Angelopoulos, V., Cruce, P., Drozdov, A., Grimes, E. W., Hatzigeorgiu, N., King, D. A., et al.: The Space Physics Environment Data Analysis System (SPEDAS), Space Sci. Rev., 215, 9, https://doi.org/10.1007/s11214-018-0576-4, 2019.

Angelopoulos, V., Lewis, J., McTiernan, J., Grimes, E., Russell, C., Drozdov, A., Cruce, P., Hatzigeorgiu, N., Wu, J., Larson, D., McFadden, J., and Flores, A.: SPEDAS (Space Physics Environment Data Analysis System) (6.1), https://doi.org/10.5281/zenodo.15023025, 2024.

Auster, H., Glassmeier, K., Magnes, W., andW. Baumjohann, O. A., Constantinescu, D., Fischer, D., Fornacon, K., Georgescu, E., Harvey, P., Hillenmaier, O., Kroth, R., Ludlam, M., Narita, Y., Nakamura, R., Okrafka, K., Plaschke, F., Richter, I., Schwarzl, H., Stoll, B., Valavanoglou, A., and Wiedemann, M.: The THEMIS Fluxgate Magnetometer, Space Sci. Rev., 141, 235–264, https://doi.org/10.1007/s11214-008-9365-9, 2008.

Balogh, A.: Planetary Magnetic Field Measurements: Missions and Instrumentation, Space Science Reviews, 152, 23–97, https://doi.org/10.1007/s11214-010-9643-1, 2010.

Edmond, J., Raeder, J., Ferdousi, B., Argall, M., and Innocenti, M. E.: Clustering of Global Magnetospheric Observations, Journal of Geophysical Research: Machine Learning and Computation, 1, e2024JH000 221, https://doi.org/10.1029/2024JH000221, 2024.

Frühauff, D., Plaschke, F., and Glassmeier, K.-H.: Spin axis offset calibration on THEMIS using mirror modes, Annales Geophysicae, 35, 117–121, https://doi.org/10.5194/angeo-35-117-2017, 2017.

Grimes, E. W., Lewis, J. W., Angelopoulos, V., McTiernan, J. M., Hatzigeorgiu, N., Drozdov, A., and Russell, C.: Pyspedas, a Python Implementation of SPEDAS, in: AGU Fall Meeting Abstracts, vol. 2018, pp. IN11B–0629, 2018.

Grimmich, N., Plaschke, F., Archer, M. O., Heyner, D., Mieth, J. Z. D., Nakamura, R., and Sibeck, D. G.: Study of Extreme Magnetopause Distortions Under Varying Solar Wind Conditions, Journal of Geophysical Research: Space Physics, 128, e2023JA031 603, https://doi.org/10.1029/2023JA031603, 2023.

Hedgecock, P. C.: A correlation technique for magnetometer zero level determination., Space Science Instrumentation, 1, 83–90, 1975.

Kepko, E., Khurana, K., Kivelson, M., Elphic, R., and Russell, C.: Accurate determination of magnetic field gradients from four point vector measurements. I. Use of natural constraints on vector data obtained from a single spinning spacecraft, IEEE Transactions on Magnetics, 32, 377–385, https://doi.org/10.1109/20.486522, 1996.

Lucek, E. A., Constantinescu, D., Goldstein, M. L., Pickett, J., Pinçon, J. L., Sahraoui, F., Treumann, R. A., and Walker, S. N.: The Magnetosheath, Space Science Reviews, 118, 95–152, https://doi.org/10.1007/s11214-005-3825-2, 2005.

Matzka, J., Stolle, C., Yamazaki, Y., Bronkalla, O., and Morschhauser, A.: The Geomagnetic Kp Index and Derived Indices of Geomagnetic Activity, Space Weather, 19, e2020SW002 641, https://doi.org/10.1029/2020SW002641, 2021.

McFadden, J., Carlson, C., Larson, D., Ludlam, M., Abiad, R., Elliott, B., Turin, P., Marckwordt, M., and Angelopoulos, V.: The THEMIS ESA Plasma Instrument and In-flight Calibration, Space Sci. Rev., 141, 277–302, https://doi.org/10.1007/s11214-008-9440-2, 2008.

Plaschke, F., Auster, H.-U., Fischer, D., Fornaçon, K.-H., Magnes, W., Richter, I., Constantinescu, D., and Narita, Y.: Advanced calibration of magnetometers on spin-stabilized spacecraft based on parameter decoupling, Geoscientific Instrumentation, Methods and Data Systems, 8, 63–76, https://doi.org/10.5194/gi-8-63-2019, 2019.

Pöppelwerth, A.: THEMIS Spin Axis Magnetic Field Reconstruction, Zenodo [software], https://doi.org/10.5281/zenodo.18594248, 2026.

THEMIS: THEMIS mission including level 2 FGM and ESA data, available at: http://themis.ssl.berkeley.edu/data/themis, last access: 27 January 2026, 2026.

Tsyganenko, N.: A magnetospheric magnetic field model with a warped tail current sheet, Planetary and Space Science, 37, 5–20, https://doi.org/10.1016/0032-0633(89)90066-4, 1989.